

# Limits on the luminosity function of Ly $\alpha$ emitters at $z = 7.7^*$

P. Hibon<sup>1,2</sup>, J.-G. Cuby<sup>1</sup>, J. Willis<sup>4</sup>, B. Clément<sup>1</sup>, C. Lidman<sup>3</sup>, S. Arnouts<sup>5,1</sup>, J.-P. Kneib<sup>1</sup>,  
C. J. Willott<sup>6</sup>, C. Marmo<sup>7</sup>, and H. McCracken<sup>7</sup>

<sup>1</sup> Laboratoire d'Astrophysique de Marseille, OAMP, Université Aix-Marseille & CNRS, 38 rue Frédéric Joliot Curie, 13388 Marseille Cedex 13, France

<sup>2</sup> Korean Institute for Advanced Study, Dongdaemun-gu, Seoul 130-722, Korea

<sup>3</sup> European Southern Observatory, Alonso de Cordova 3107, Vitacura, Casilla 19001, Santiago 19, Chile

<sup>4</sup> Department of Physics and Astronomy, University of Victoria, Elliot Building, 3800 Finnerty Road, Victoria, BC, V8P 5C2, Canada

<sup>5</sup> Canada France Hawaii Telescope Corporation, Kamuela, HI 96743, USA

<sup>6</sup> Herzberg Institute of Astrophysics, National Research Council, 5071 West Saanich Rd, Victoria, BC V9E 2E7, Canada

<sup>7</sup> Institut d'Astrophysique de Paris, Université Pierre et Marie Curie, 98bis boulevard d'Arago, 75014 Paris, France

Received 19 March 2009 / Accepted 13 January 2010

## ABSTRACT

**Aims.** The Ly $\alpha$  luminosity function (LF) of high-redshift Ly $\alpha$  emitters (LAEs) is one of the few observables of the re-ionization epoch accessible with 8–10 m class telescopes. The evolution of the LAE LF with redshift is dependent upon the physical evolution of LAEs and the ionisation state of the Universe towards the end of the Dark Ages.

**Methods.** We performed a narrow-band imaging program at 1.06  $\mu\text{m}$  using CFHT/WIRCcam. The observations target Ly $\alpha$  emitters at redshift  $z \sim 7.7$  in the CFHT-LS D1 field. From these observations we derived a photometric sample of 7 LAE candidates at  $z \sim 7.7$ .

**Results.** We derive luminosity functions for the full sample of seven objects and for subsamples of four objects. Assuming the brightest objects in our sample are real, we find that the resulting luminosity function is not consistent with previous work at lower redshifts. More definitive conclusions will require spectroscopic confirmation.

**Key words.** early Universe – galaxies: luminosity function, mass function – galaxies: high-redshift

## 1. Introduction

Searching for high-redshift galaxies is one of the most active fields in observational cosmology. The most distant galaxies provide a direct probe of the early stages of galaxy formation, in addition to revealing the effects of cosmic re-ionization (Fan et al. 2006). The brightest galaxies at  $z \sim 6$  (Eyles et al. 2007) indicate that star formation commenced at significantly higher redshifts and that such galaxies are likely to contribute significantly to re-ionization. Conversely, detection of  $z > 7$  galaxies is still rare, in large part because of the complete absorption of their restframe UV emission below the Ly $\alpha$  line which is redshifted beyond the 1  $\mu\text{m}$  cutoff wavelength of silicon. The deployment of large format IR arrays at many telescopes now makes these observations possible. From  $z = 6.5$  to  $z = 7.7$ , light dimming due to luminosity distance is 30% and the age of the Universe decreases by 150 Myr, leading to further dimming due to age, probably moderate considering the relatively short time span. Observations of  $z > 7$  objects should therefore remain within reach of the current generation of telescopes.

\* Based on observations obtained at the Canada-France-Hawaii Telescope (CFHT), which is operated by the National Research Council (NRC) of Canada, the Institut National des Sciences de l'Univers of the Centre National de la Recherche Scientifique of France (CNRS), and the University of Hawaii. This work is based in part on observations obtained with MegaPrime/MegaCam, a joint project of CFHT and CEA/DAPNIA and in part on data products produced at TERAPIX and the Canadian Astronomy Data Centre as part of the Canada-France-Hawaii Telescope Legacy Survey, a collaborative project of NRC and CNRS.

One prime tracer of high-redshift galaxies is the Ly $\alpha$  line. The determination of the Ly $\alpha$  luminosity function (LF) with infrared arrays is being actively pursued by several groups, either through narrow-band imaging (e.g. Willis et al. 2008; Cuby et al. 2007) or through blind spectroscopy along the critical lines of galaxy clusters used as gravitational telescopes (Richard et al. 2006; Stark et al. 2007; Bouwens et al. 2008). High- $z$  galaxies are also being discovered using the dropout technique between the optical and near infrared domains, either in the field (see e.g. Bouwens et al. 2009) or behind galaxy clusters (see e.g. Richard et al. 2008). The dropout method is primarily sensitive to the UV continuum emission of the galaxies and therefore allows to determine their UV luminosity function (UVLF).

The UVLF of LAEs is a direct tracer of galaxy evolution and it is not affected by the amount of neutral hydrogen in the intergalactic medium (IGM), while the Ly $\alpha$  emission (and therefore the Ly $\alpha$  LF) may be affected. A rapid change in the ionization state of the Universe could lead to a decline in the Ly $\alpha$  luminosity density at high redshift, while the UVLF should have a milder evolution. Evidence of such rapid change of the neutral fraction of the IGM between redshifts 6 and 7 includes the observation of LAEs in narrow-band imaging at  $z = 6.5$  (Kashikawa et al. 2006) and at  $z = 7$  (Ota et al. 2008) and in spectroscopy at  $z > 7$  (Richard et al. 2008). The patchy structure of a partially ionized Universe should also affect the apparent clustering of LAEs at high redshifts; see Mesinger & Furlanetto (2008) for an analysis of this effect at  $z \sim 9$ .

More observations of LAEs at high redshifts are needed to better characterize the re-ionization epoch, and in particular

observations in the near-IR domain to probe redshifts  $\gtrsim 7$ . Willis & Courbin (2005), Willis et al. (2008) and Cuby et al. (2007) have performed narrow-band surveys at  $z = 8.8$  that yielded only upper limits of the Ly $\alpha$  LF of LAEs at this redshift. In this paper we present the results of a narrow-band imaging survey at  $z = 7.7$  representing a factor of 10 improvement in area at approximately the same detection limit compared to our previous survey at  $z = 8.8$ . These observations were made with the Wide Field near-IR Camera (WIRCam) operating at CFHT<sup>1</sup>.

In Sect. 2, we describe the narrow-band observations and other data used in this paper. In Sect. 3, we discuss the construction of our sample of Ly $\alpha$  emitters. In Sect. 4, we compute the Ly $\alpha$  luminosity function of  $z = 7.7$  LAEs and compare it to the results of other surveys and to simulations.

Unless explicitly stated otherwise, we use AB magnitudes throughout the paper. We assume a flat,  $\Lambda$ CDM model with  $\Omega_M = 0.27$  and  $H = 70 \text{ km s}^{-1} \text{ Mpc}^{-1}$ .

## 2. Observational data

The CFHT-LS D1 field provides imaging data from X-ray to near-IR wavelengths, including extremely deep optical data from the CFHT Legacy Survey. For the purpose of this study, we originally made use of the T0004 catalog release of the CFHT-LS survey, and later of the T0005 release when it became available (November 2008). The CFHT-LS data products are available from the CADC archive to CFHT users and take the form of image stacks in the  $u^*g'r'i'z'$  filters and of ancillary data, such as weight maps, quality checks, catalogs, etc. The  $u^*, g', r', i', z'$  filters have spectral curves similar to the SDSS filters.

The core data relevant to this paper are deep ( $\sim 40$  h) near-IR Narrow Band (NB) observations of a  $\sim 20' \times 20'$  area of the CFHT-LS D1 field. In addition to the narrow-band near-IR data we employed broad band  $J, H$  and  $K_s$  data of the same field acquired as part of another program carried out with WIRCam Deep Survey (WIRDS; PIs Willott & Kneib). We also used near-IR Spitzer/IRAC data from the SWIRE survey (Lonsdale et al. 2003).

A summary of the observational data used in this paper is provided in Table 1. Figure 1 shows the transmission curves of the filters corresponding to the multi-band data used in this paper.

### 2.1. WIRCam narrow-band data

WIRCam is a  $\sim 20' \times 20'$  imager installed at the CFHT prime focus. It is equipped with 4 Hawaii2-RG arrays with a pixel scale of  $0.3'' \text{ pixel}^{-1}$ . The four arrays are separated by a  $\sim 15''$  gap. We used the Low-OH1 filter centered at  $1.06 \mu\text{m}$  (hereafter referred to as NB1060) with a full width at half maximum of  $0.01 \mu\text{m}$  ( $\sim 1\%$ ). The wavelength response of this filter is located within a spectral region of low night sky OH emission.

The data were acquired in queue mode over several months in two different semesters in 2005B and 2006B with each epoch totalling approximately  $\sim 20$  h of integration time. A detector integration time of 630 s per frame was selected to provide background limited performance. The sky background was measured to be  $\sim 4e^- \text{ s}^{-1} \text{ pixel}^{-1}$ , corresponding to a sky brightness  $\sim 17.7 \text{ mag arcsec}^{-2}$  (Vega). Our first observations started shortly after the commissioning of the camera. At this time the detector was experiencing variable readout noise and significant

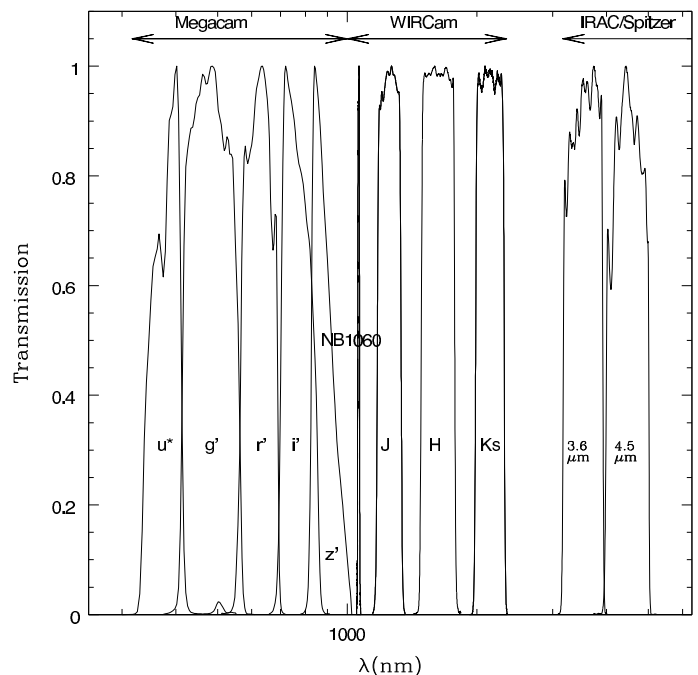


**Fig. 1.** Transmission curves of the filters corresponding to the data used in this paper. All transmissions are normalized to 100% at maximum.

**Table 1.** Observational data.

Instrument	Band	Integration time (h)	Limiting magnitude <sup>a</sup>
MegaCam	$u^*$	20.7	27.9
MegaCam	$g'$	25	28.1
MegaCam	$r'$	49	27.8
MegaCam	$i'$	74	27.4
MegaCam	$z'$	55.8	26.5
WIRCam	NB 1st epoch	20	24.8
WIRCam	NB 2nd epoch	20	24.9
WIRCam	NB combined	40	25.2
WIRCam	$J$	6.2	25.0 <sup>b</sup>
WIRCam	$H$	7.7	24.7
WIRCam	$K_s$	8.9	24.7 <sup>b</sup>
IRAC	$3.6 \mu\text{m}$	0.034	22.2
IRAC	$4.5 \mu\text{m}$	0.034	21.5

**Notes.** <sup>(a)</sup>  $4\sigma$  magnitude limits in apertures  $1.5''$  in diameter for MegaCam and WIRCam. These limits correspond to a 50% completeness level. IRAC limiting magnitudes are  $5\sigma$  in  $3.8''$  apertures. <sup>(b)</sup> In one quarter of the field, for which additional NTT/SOFI data were available, magnitude limits of 25.2 in  $J$  and 24.8 in  $K_s$  were achieved.

electronic crosstalk, both issues that were progressively solved in the subsequent months of operations. The 2005B data were therefore the most significantly affected. We discuss the potential effects of the electronic cross-talk as a source of contamination in Sect. 3.3.1.

When observing with WIRCam telescope guiding is achieved through the on-chip guiding capability implemented in the detector controller. This is performed by clocking small detector windows around bright stars for fast readout and rapid guiding. This feature does also leave some residuals on the images along the detector lines where the windows are located.

The narrow-band data were pre-processed at CFHT (dark subtraction and flat fielding). The pre-processed images were then stacked together at the Terapix data processing center at Institut d'Astrophysique de Paris (IAP). The data reduction steps

<sup>1</sup> See <http://www.cfht.hawaii.edu/Instruments/Imaging/WIRCam/>

include double pass sky subtraction, astrometric and photometric calibration and final stacking of the images. Two separate stacks were produced for each of the one-year datasets. Details of the data reduction are presented in Marmo (2007). We combined these two stacks into a single stack corresponding to the entire dataset. The area of the final stacked image after removal of the edges was  $390 \text{ arcmin}^2$  and the *FWHM* of stellar sources was measured to be  $\sim 0.76''$ .

## 2.2. WIRCam Broad band data

The broad band *J*, *H* and *K<sub>s</sub>* WIRCam data were acquired in 2006B and 2007B and were processed in a manner similar to the narrow-band data. Moderately deep SOFI (ESO-NTT) *J* and *K<sub>s</sub>* band images were also available, covering one quarter of the WIRCam field (Iovino et al. 2005). The SOFI data increased the limiting magnitude of the survey by 0.1 to 0.2 mag in the *J* and *K<sub>s</sub>* bands for the corresponding quadrant. We did not use data from the UKIDSS Deep Extragalactic Survey (UKIDSS-DXS; Lawrence et al. 2007) *J*, *H* and *K<sub>s</sub>* images as these data are less deep than those acquired by our program. The image quality measured in the *J* and *K<sub>s</sub>* images is comparable to that of the *NB1060* image.

We emphasize at this point that the spectral response of the *NB1060* and *J* WIRCam filters do not overlap. The wavelengths of the blue and red ends of the full width at half maximum of the *J* filter are 1175 and 1333 nm. The *J* filter can therefore be used to trace the UV continuum above the Ly $\alpha$  line without being contaminated by line emission.

## 2.3. Photometric calibration

Photometric calibration of the NB data set is complicated by the fact that photometric reference sources do not currently exist for the *NB1060* filter and no spectrophotometric standard stars were observed as part of the program. We therefore employed spectral fitting of stars identified in the science image to determine the NB zero point. For consistency we applied identical procedures for the photometric calibration of the entire MegaCam and WIRCam datasets. We selected stars as morphologically unresolved, non-saturated sources from the source catalogues. Some 75 of these sources were matched with sources present in the 2MASS catalog. We determined the zero points of the WIRCam broad band data (*J* and *K<sub>s</sub>*) by minimizing the difference between the WIRCam and 2MASS magnitudes of this stellar sample. This procedure generated rms residuals of 0.07 and 0.15 mag in the *J* and *K<sub>s</sub>* bands respectively.

For the MegaCam data, we applied zero point offsets up to 0.06 magnitudes to the photometric catalog distributed as part of the T0004 CFHT-LS release. These offsets were determined by Ilbert et al. (2006) when fitting the original CFHT-LS photometry to synthetic colors of galaxies derived from SED models as part of a photometric redshift analysis. These offsets were originally determined for the T0003 release, and we used slightly modified ones corresponding to the T0004 release (Coupon et al. 2009; Ilbert et al. 2006).

In addition to the above approach, we generated synthetic colors for the MegaCam and WIRCam filters of a variety of stellar spectra models of various temperatures and metallicities (Marigo et al. 2008, and <http://stev.oapd.inaf.it/~lgirardi/cgi-bin/cmd>). The WIRCam *J* and *K<sub>s</sub>* magnitudes of the stellar sample provided a satisfactory match to the synthetic color tracks. However, the CFHT-LS magnitudes had

to be modified by offsets of similar magnitude to those mentioned above to provide a better match to the color tracks. This suggests that there are systematic offsets between the CFHT-LS photometry and synthetic colors of stars and galaxies. It is not surprising that the photometric offsets for stars and galaxies are similar as synthetic SED modeling of galaxies makes direct use of stellar spectra. It is perhaps more interesting that these offsets do not appear to depend upon the models considered (as noted by Ilbert et al. 2006) a fact which is supported by our analysis using completely different synthetic stellar libraries.

We performed a final check using the stellar library of Pickles (1998). This library consists of observed stellar spectra in the optical and parts of the near-IR domain with interpolated points computed in unobserved spectral regions. Once again the MegaCam color tracks computed using the Pickles library match the observed colors of our stellar sample after applying the same offsets as above.

From the color tracks we determined that the stars of the stellar sample used for calibration have spectral types from G to M5. Then, from the calibrated  $u^*$ ,  $g'$ ,  $r'$ ,  $i'$ ,  $z'$ , *J*, *H* and *K<sub>s</sub>* data, we performed an ad hoc polynomial fitting of the fluxes of all objects in the stellar sample, from which we derived for each star the *NB1060* magnitude at  $1.06 \mu\text{m}$ . This simple method is justified in view of the large number of photometric datapoints (7) available, of the smooth spectral energy distribution of stars, and of the absence of features at the wavelength of the *NB1060* filter in the infrared spectra of stars of spectral types earlier than M5.

The computed stellar reference magnitudes were applied to determine the zero point of the *NB1060* image. The zero point magnitude in each quadrant was computed individually as each displays a slightly different electronic gain. The typical rms residual in each quadrant after this last step was 0.04 mag.

Making provision for additional sources of errors, e.g. the accuracy of the 2MASS photometry, possible biases from the selected sample of stars, etc., we estimate our final photometric accuracy to be on the order of 0.1 mag rms and we adopt this value in the rest of this paper.

## 2.4. Catalog generation and detection limits

We used SExtractor (Bertin & Arnouts 1996) in single image mode for object detection and photometry in the *NB1060*, *J*, *H* and *K<sub>s</sub>* WIRCam images. The magnitudes were computed in apertures 5 pixels ( $1.5''$ ) in diameter. We used the CFHT-LS public images of the field for the optical  $u^*g'r'i'z'$  bands, photometrically corrected as explained in the previous section.

The limiting magnitude of the *NB1060*, *J*, *H* and *K<sub>s</sub>* WIRCam observations was estimated as follows: we added 200 artificial star-like objects per bin of 0.1 mag onto the stacked *NB1060* image in carefully selected blank regions. We then ran SExtractor on this image using the same parameters as previously used for object detection. Counting the number of artificial stars retrieved in each magnitude bin provided a direct measure of our completeness limit. The limiting magnitude that we report in this paper corresponds to the 50% completeness limit.

When analysing the optical data we re-binned the original CFHT-LS images with a pixel scale  $0.19'' \text{ pixel}^{-1}$  to the  $0.3'' \text{ pixel}^{-1}$  scale of the WIRCam images. We then ran SExtractor with the same parameters used with the WIRCam data. We checked that the photometry before and after re-binning was preserved. We then computed the 50% completeness limit for the CFHT-LS images using the approach that was applied to the WIRCam images.

In order to estimate the signal to noise ratio ( $SNR$ ) of our candidates and the  $SNR$  corresponding to our 50% completeness limit we used the noise image (BACKGROUND\_RMS) produced by SExtractor. This image details the local noise  $\sigma$  per pixel. The  $SNR$  of an object with  $F$  counts in an aperture of  $A$  pixels is given by

$$SNR = F / \sqrt{A\sigma^2}, \quad (1)$$

with the error on the magnitude  $m$  given by:

$$\Delta m = 1.086/SNR. \quad (2)$$

The limiting magnitude at 50% completeness of the  $NB1060$  image computed using the above method is 25.2. This magnitude corresponds to a source of  $SNR \sim 4$  and a NB flux of  $8.3 \times 10^{-18} \text{ erg s}^{-1} \text{ cm}^{-2}$ .

A similar procedure was used to derive the limiting magnitudes of all CFHT-LS and WIRCam images. They are reported in Table 1.

### 3. Sample construction

#### 3.1. Initial candidate selection

We created a catalog of multi-band photometry for detected sources by matching sources detected in individual bands to those detected in the  $NB1060$  image using a matching tolerance of  $0.7''$ .

Our initial selection of  $Ly\alpha$  candidates was based on the following criteria:

1. We selected objects detected in the  $NB1060$  image yet absent in all optical images ( $u^*$ ,  $g'$ ,  $r'$ ,  $i'$ ,  $z'$ ), assuming that no flux will be detected blueward of the  $Ly\alpha$  line. Negligible amounts of radiation are expected to escape the galaxy and to be transmitted by the IGM below the  $z = 7.7$  Lyman limit at  $\sim 790 \text{ nm}$ . This means no flux in the  $u^*$ ,  $g'$  and  $r'$  bands. All the radiation between the  $Ly\alpha$  and  $Ly\gamma$  lines at  $z = 7.7$  is entirely redshifted beyond the Gunn-Peterson (GP) trough at  $\sim 850 \text{ nm}$  observed in the spectra of high-redshift quasars (Fan et al. 2006), and which corresponds to  $Ly\alpha$  absorption by the partially neutral IGM above  $z \sim 6$ . There should therefore be no detectable flux in the  $z'$  band and limited flux in  $i'$  band with a very strong color break  $i' - J \gtrsim 3$  (Becker et al. 2001).
2. We required that the  $NB1060$  objects detected in the combined image were also detected in each of the  $NB1060$  stacks corresponding to each observing semester. While each half-stack is at lower  $SNR$  than the combined image used for generating the master  $NB1060$  catalog, this criterion permits the removal of variable (in flux or in position) objects and reduces considerably the number of low  $SNR$  detections.
3. We required a signal to noise ratio of  $\sim 5$  or higher on the combined image, corresponding to a  $SNR \gtrsim 3.5$  in half stack images.

Considering the limiting magnitude of our optical and NB images, the first selection criterion corresponds to:

$$\begin{aligned} u^* - NB1060 &> 2.7 \\ g' - NB1060 &> 2.9 \\ r' - NB1060 &> 2.6 \\ i' - NB1060 &> 2.2 \\ z' - NB1060 &> 1.3. \end{aligned} \quad (3)$$

Taken altogether, the color break between the optical and  $NB1060$  filters is extremely high and covers a wide spectral range. For the CFHT-LS, the Terapix data center generated deep  $\chi^2$  images combining the  $g'$ ,  $r'$  and  $i'$  images. Without entering into considerations on wide band/multi-color magnitudes, we can infer from equations 3 that the optical dropout selection can be broadly expressed as:

$$g'r'i' - NB1060 \gtrsim 3. \quad (4)$$

We remark that this color break is significantly stronger than what has been usually in previous high- $z$  LAEs or LBGs searches, although with a slight gap in wavelength between the optical red end and the  $NB1060$  filter.

Having applied these criteria, careful visual inspection of the candidates allowed us to remove a few obvious fake candidates in the form of electronic ghosts or artifacts around bright stars. A couple of objects of dubious quality in one or more of the images, or those with unusual morphologies, were also removed.

Finally, three bright  $K_s$  band sources with  $NB1060 - K_s \gtrsim 1.2$  were flagged as Extremely Red Objects (EROs) (see also Sect. 3.3.6) and were discarded. This corresponds to an additional color selection criterion for the candidates:

$$NB1060 - K_s \lesssim 1.2. \quad (5)$$

Application of these criteria generated an initial list of 8 objects, none of them are resolved at the level of the image quality of the  $NB1060$  image ( $0.76''$ ).

Finally, we note that none of the objects in our list have counterparts in the Spitzer/IRAC SWIRE data of the same field. Even if the  $H\alpha$  line was  $\sim 100$  times brighter than the  $Ly\alpha$  line, it would remain undetected in the  $5.8 \mu\text{m}$  IRAC band SWIRE data.

#### 3.2. The sample

Our sample consists of 8 objects listed in Table 2 and shown in Fig. 2. Five objects have  $NB1060 - J < 0$  and are flagged as candidate emission line objects. One has  $NB1060 - J \sim 0$  and therefore does *not* qualify as an emission line object. It is instead identified as a T-dwarf candidate (see Sect. 3.3.5). The two remaining objects are NB-only detections and cannot be unambiguously identified as line emitting objects.

Therefore, from the six brightest objects of the original sample of eight selected without using the  $J$  magnitudes, five appear to be line emitters. With the same success rate of 5/6 the two faintest objects should therefore also be line emitters and it is therefore reasonable to keep them in the final sample – although noting that the identification is less secure than the other candidates.

We also report in Table 2 the lower limits of the restframe equivalent widths ( $EW$ ) derived from the photometric data, defined as:

$$EW_{\text{rest}} = \left( \frac{f_{\lambda, NB1060} \times \lambda_{NB1060}^2}{f_{\lambda, J} \times \lambda_J^2} - 0.5 \right) \times \frac{\Delta\lambda_{NB1060}}{1+z} \quad (6)$$

where  $f_{\lambda}$  is the observed flux density in  $\text{erg s}^{-1} \text{ cm}^{-2} \text{ \AA}^{-1}$  at the wavelengths of the  $NB1060$  and  $J$  filters and  $\Delta\lambda_{NB1060}$  is the width of the  $NB1060$  filter ( $100 \text{ \AA}$ ). It is assumed that the UV continuum is completely absorbed below the  $Ly\alpha$  line, and therefore contributes to the  $NB1060$  flux over one half of the filter spectral width. We assume a constant continuum flux density in  $f_{\nu}^2$ . Six out of seven of our LAE photometric candidates are not

<sup>2</sup> Taking a constant flux density in  $f_{\lambda}$  would lead to  $EW$  values that are approximately twice as large.

**Table 2.** Table of the  $z \sim 7.7$  LAE and T-dwarf candidates.

Name	NB1060	Error	SNR (NB1060)	$J$	Error	$SNR(J)$	$H$	Error	$SNR(H)$	$K_s$	$EW^a$ (Å)
LAE#1	24.0	0.08	14.5	24.5	0.16	6.7	24.7	0.3	4	>24.7	13
LAE#2	24.3	0.17	6.5	>25.0	...	...	>24.7	...	...	>24.7	>16
LAE#3	24.6	0.15	7.2	>25.2	...	...	>24.7	...	...	>24.8	>15
LAE#4	24.8	0.19	5.8	>25.2	...	...	>24.7	...	...	>24.8	>11
LAE#5	24.9	0.2	5.5	>25.2	...	...	>24.7	...	...	>24.8	>9
LAE#6 <sup>b</sup>	25.1	0.19	5.9	>25.0	...	...	>24.7	...	...	>24.7	>5
LAE#7 <sup>b</sup>	25.1	0.22	4.9	>25.0	...	...	>24.7	...	...	>24.7	>5
TDW#1 <sup>c</sup>	24.3	0.12	9.4	24.2	0.15	7.3	>24.7	...	...	>24.7	...

**Notes.** <sup>(a)</sup> In the restframe. <sup>(b)</sup> These two objects are not unambiguously identified as line emitting objects, but are included in the LAE sample (see text for details). <sup>(c)</sup> This object is not formally part of the sample because it is a likely late type T-dwarf (see text for details).

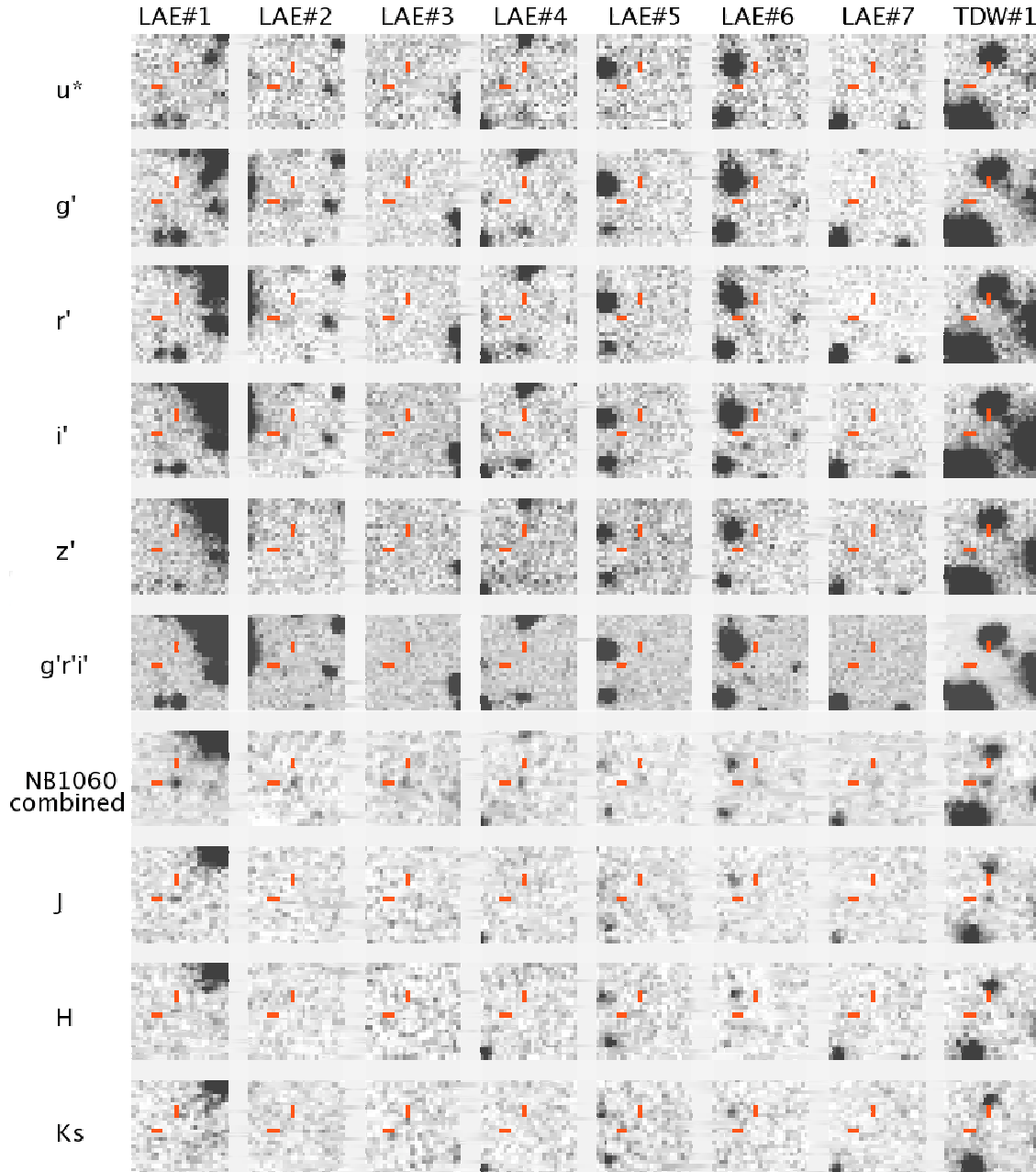


**Fig. 2.** Thumbnail images of all candidates listed in Table 2. Object TDW#1 is displayed for reference but is not part of the LAE sample (see text for details). Objects names and passbands are located above and to the left of the thumbnails, respectively.

detected in the  $J$  band and we therefore use the detection limit in this band, deriving in turn lower  $EW$  limits. We note that LAE#6 and LAE#7 have positive  $EW$  limits despite the fact that their  $NB1060$  magnitudes are fainter than their  $J$  magnitudes.

Samples of emission line selected galaxies are normally defined in terms of the equivalent width sampled by a particular survey. For example, Taniguchi et al. (2005) present a sample of 9 spectroscopically confirmed LAEs at  $z = 6.5$  with  $EW$  values  $EW_{\text{obs}} > 130 \text{ \AA}$  or  $EW_{\text{rest}} > 17 \text{ \AA}$ . In our sample of candidate  $z = 7.7$  LAEs, the faintest line emitter (LAE#5) presents  $NB1060 - J < -0.3$  which corresponds to an  $EW$  limit  $EW_{\text{obs}} > 80 \text{ \AA}$  or  $EW_{\text{rest}} > 9 \text{ \AA}$ . Considering that, in all but one case, the  $EW$  values are lower limits, the lower range of  $EW$ s sampled by our observations is comparable to that of other studies. Within the practical limitation of matching the selection criteria of two different surveys, the two populations of LAEs revealed by Taniguchi et al. (2005) and the current study are therefore approximately equivalent in terms of the  $EW$  sampled. However, the  $z = 7.7$  LAEs presented in this paper are selected to be  $NB1060$  excess sources at a lower significance level than the Taniguchi et al. (2005) LAEs. Moreover, our sources are not confirmed spectroscopically. Therefore, when comparing the LF properties of the  $z = 7.7$  LAE candidates to confirmed LAE sources at  $z = 6.5$ , we must include an assessment of the unknown sample contamination.

### 3.3. Possible sources of contamination

Known astronomical objects such as extremely red objects or T-dwarfs can potentially satisfy the optical dropout selection and therefore contribute to our sample. We examine various such examples of contamination in this section, in addition to contamination from instrumental sources.

In the discussion that follows we will make use of Fig. 3, which shows the  $NB1060 - K_s$  versus  $NB1060 - J$  colors of the candidate LAEs together with the colours of possible contaminating sources.

We used the template spectra (without emission lines) described in Ilbert et al. (2009). Spectra were redshifted over the interval  $0 < z < 8$  and reddened according to a range of  $E(B - V)$  values over the interval  $0 < E(B - V) < 5$ . This process generated approximately 100,000 spectra. We then applied our selection criteria (Eq. (3)) to this spectral sample and computed  $NB1060 - J$  and  $NB1060 - K_s$  colors. The envelope of points corresponding to galaxies at redshifts  $z < 6$  ( $z > 6$ ) is indicated by the dark (light) grey zone in Fig. 3.

#### 3.3.1. Electronic crosstalk

The WIRCam detectors suffer from relatively strong electronic cross-talk. The effect is manifest as the appearance of ghost images every 32 rows or columns around bright and saturated stars. Three types of electronic ghosts have been identified: positive, negative and ‘‘edge’’ ghosts, the latter consisting of spot images positive on one edge and negative on the other edge. The pattern of these electronic ghosts follows the pattern of objects on each image, as the effect is caused by (bright) objects. Only the positive ghosts are likely to generate false candidates. They are however easily recognizable as they are distributed along columns with a fixed pattern originating from the brightest stars. Median filtering over every 32nd row (which corresponds to the number of amplifiers) allows one to identify and reject the ghosts while retaining the astronomical objects. Having applied this

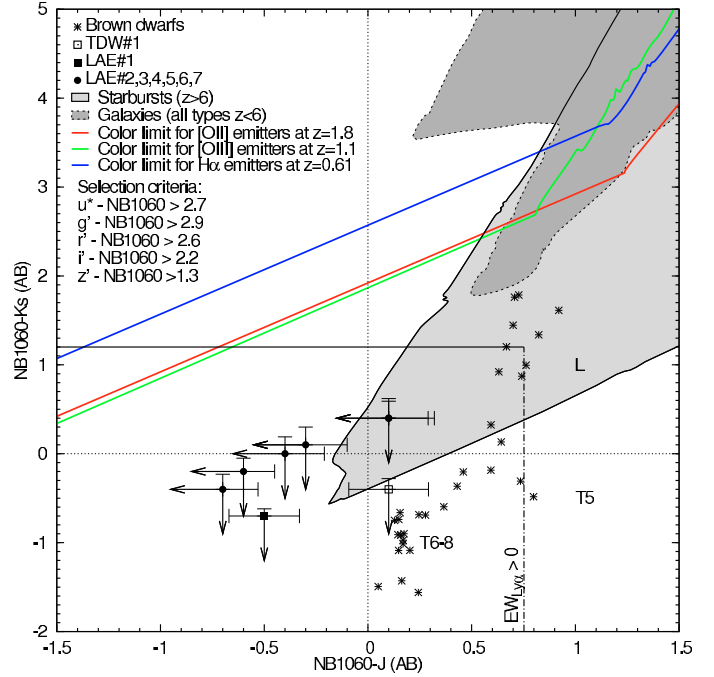


**Fig. 3.**  $NB1060 - J$  and  $NB1060 - K_s$  color-color diagram. The filled square symbol corresponds to LAE#1, the filled circles to LAE candidates #2 to #7, and the open square to the T-dwarf candidate. Photometric errors are represented by the error bars or arrows depending on whether the objects are detected or not in the  $J$  and/or  $K_s$  bands. Star symbols correspond to L and T-dwarfs (see Sect. 3.3.5). The grey areas correspond to the colors of  $z > 6$  starbursts and  $z < 6$  galaxies with reddening values  $E(B - V)$  in the range  $[0-5]$  that satisfy the color selection criteria used in this work. The template spectra used to compute the colors are described in Ilbert et al. (2009) and are without emission lines. The result of adding an emission line to the spectra is to move the points to the left of the plot parallel to a line of slope 1. The lines drawn from the bluest  $NB1060 - K_s$  datapoints at redshifts 0.61 (blue), 1.1 (green) and 1.8 (red) are indicated. Emission line galaxies at these redshifts are located above these lines.

procedure, the data were carefully inspected and 2 additional objects were subsequently discarded as electronic ghosts as they presented several similarities with the appearance of brighter ghosts.

#### 3.3.2. Persistence

Pixels illuminated by bright stars in one image continue to release electrons long after the illumination has stopped. This generates fake objects at the positions once illuminated by these stars. These fake sources remain fixed on the detector and therefore do not follow the objects during the dithering pattern. In principle, they are removed by sigma or min-max clipping when the images are stacked, however faint residuals may remain. Indeed, a pattern of faint objects reproducing the pattern of telescope offsets was observed around the brightest stars in the image, generating false candidates which could be easily identified and removed.

#### 3.3.3. Noise

Following the approach outlined in Iye et al. (2006), we estimate that there are  $\sim 10^6$   $1.5''$  (diameter) circular apertures in our NB data. Assuming a Gaussian distribution, the corresponding number of false alarm events above  $5\sigma$  is  $\sim 0.3$ . This is

admittedly an analysis that does not take into account the fact that the noise properties of the stacked and resampled NB image deviate from a Gaussian distribution. While contamination from noise might take place close to the detection limit, noise is not a plausible source of contamination for higher SNR objects.

### 3.3.4. Transient objects

At the flux limit of the survey, distant supernovae can be visible for several weeks, and are therefore a potential source of contamination. We computed the expected number of type Ia and type II supernovae that would be visible in our narrow-band WIRCam images by using the method presented in [Cuby et al. \(2007\)](#). For a limiting magnitude of 24.8, which corresponds to the depths reached in the one-year stacked images (see Table 1), we find that  $\sim 3$  supernovae would have occurred in the area covered by our data. While contamination by SNe is probable in the individual one-year stacks, such objects are automatically removed from our final list of candidates because of the constraint that they be present in both one-year images. Similarly, stacking of data acquired over long time spans automatically removes slowly moving solar-system objects.

### 3.3.5. T-dwarfs

Using the [Tinney et al. \(2003\)](#) spectral type vs. absolute magnitude relations, we calculate that we could detect T-dwarfs up to distances of 300 to 1000 pc, depending on spectral type, from the coolest to the warmest. Considering the high galactic latitude of our field, this extends our sensitivity to T-dwarfs far beyond the scale height of the Galactic disk. Truncating to a height of 350 pc, which is the scale height that is applicable to T-dwarfs ([Ryan et al. 2005](#)), we estimate a sample volume of  $\sim 400$  pc<sup>3</sup>. Considering a volume density of T-dwarfs of a few  $10^{-3}$  pc<sup>-3</sup>, we expect no more than one T-dwarf in our field. At a couple of hundreds of parsecs from the Sun, the proper motion of these objects would not be detected over a one year timescale.

We used the public library of L and T-dwarfs spectra compiled by Burgasser (<http://web.mit.edu/ajb/www/tdwarf/>) to compute the  $NB1060 - J$  colors expected for these objects. Including T-dwarfs as late as T8 (for which NIRC spectra are available), the colours satisfy (see Fig. 3):

$$(NB1060 - J)_{T-dwarfs} > 0. \quad (7)$$

One of the brightest candidates detected in the  $J$  band has  $NB1060 - J$  colors satisfying this criterion and is therefore classified as a late-type T-dwarf (TDW#1). LAE#6 and #7 have  $NB1060 - J$  upper limits consistent with late-type T-dwarfs. However, because (i) these are only upper limits; (ii) we are not expecting many T-dwarfs in our data (see Sect. 3.3.5); and (iii) these two objects are likely to be line emitters (see Sect. 3.2), we assume, for the rest of this paper, that only TDW#1 is a T-dwarf. We show in Sect. 3.3.8 that TDW#1 could, in principle, be a high-redshift Lyman Break Galaxy, but this is less likely.

### 3.3.6. Extremely red objects

Extremely red objects (EROs) are usually defined by their  $R - K$  color, e.g.  $R_{AB} - K_{AB} \gtrsim 3.4$ , possibly with additional color criteria ([Cimatti et al. 2002](#)). They are generally identified as either old, passively evolving, elliptical galaxies or dusty starburst galaxies ([Pierini et al. 2004](#); [Bergström & Wiklind 2004](#)). Despite their faintness in the optical bands, the vast majority of

**Table 3.** Extremely red objects.

Name	$NB1060^a$	Error	$K_s^a$	Error	Size <sup>a</sup>
ERO#1	25.1	0.4	22.5	0.1	3.3
ERO#2	24.2	0.3	23	0.1	1.9
ERO#3	24.2	0.3	22.5	0.15	1.3

**Notes.** <sup>(a)</sup> MAG\_AUTO as given by SExtractor. <sup>(b)</sup> FWHM in arcsec in the  $K_s$  band.

the ERO population present in our data are detected in the  $r'$ ,  $i'$  or  $z'$  bands, and are therefore not selected as LAE candidates. Only 3 objects that passed our initial selection criteria were identified as EROs based on their bright red  $NB1060 - K_s$  colors. All three are spatially resolved. Their  $K_s$  magnitudes and sizes are given in Table 3. After removing these 3 objects from our sample, none of the remaining candidates are detected in the  $K_s$  band. The  $K_s$ -band data, although of limited depth, do provide a reasonably robust way of discriminating EROs from LAE candidates.

### 3.3.7. Low redshift emitters

Our candidates exhibit a very strong color break of about three magnitudes between the optical part of the spectrum and  $1.06 \mu\text{m}$  (Eq. (4)). Contamination could occur from strongly star-forming low-metallicity galaxies that have an emission line redshifted into the bandpass of the NB filter and an underlying continuum so faint that it would remain undetected in any of the optical broadband filters. The most likely sources of low redshift contamination are from  $H\alpha$  emitters at  $z = 0.61$ , [O III] emitters at  $z = 1.1$  and [O II] emitters at  $z = 1.8$ . We first make use of Fig. 3 to evaluate the  $EW$  of the emission lines required at these redshifts to contaminate our sample. Such emission line galaxies are located above the colored lines. For their near-IR colors to be consistent with our data (to the extreme left of the plot), the contribution of the emission lines to the  $NB1060$  flux is equivalent to restframe equivalent widths of several hundreds or thousands of Angstroms. We now discuss each source of contamination in turn.

#### $H\alpha$ emitters at $z = 0.61$

To estimate the number of  $H\alpha$  emitters present in our WIRCam image, we use the  $H\alpha$  luminosity function of [Tresse et al. \(2002\)](#) without reddening correction. To our detection limit, and assuming that the NB flux is dominated by the  $H\alpha$  line flux, we estimate that we have  $\sim 300$   $H\alpha$  emitters in the redshift interval [0.607–0.623]. The vast majority of these emitters are bright in the optical and therefore not selected.

Using the [Ilbert et al. \(2005\)](#) luminosity functions in the rest-frame UBV filters and in the redshift bin [0.60–0.8] we estimate the limiting magnitude providing 300 objects in the comoving volume sampled by the  $H\alpha$  line through the  $NB1060$  filter. We obtain magnitudes of 25.8, 26 and 25.6 corresponding approximately to the  $r'i'z'$  filters at redshift 0.6, i.e. more than 1.5 mag brighter than the limiting magnitudes of the CFHT-LS in the  $r'$  and  $i'$  filters. No normal  $z = 0.61$  galaxy spectral energy distribution can therefore contaminate our sample.

In the extreme case of a pure emission line spectrum, the sensitivity limits in the  $r'$  and  $i'$  bands correspond to [O II] and [O III] flux limits of  $3 \times 10^{-18}$  erg s<sup>-1</sup> cm<sup>-2</sup> and  $2 \times 10^{-18}$  erg s<sup>-1</sup> cm<sup>-2</sup>, respectively. Assuming an intrinsic Balmer decrement of 2.8 for case B recombination, these flux limits correspond to upper limits on the [O II]/ $H\beta$  and [O III]/ $H\beta$  line

ratios of 1.0 and 0.71, respectively. In the sample of galaxies between redshifts 0.4 and 3 presented in [Maier et al. \(2006\)](#), no objects meet these criteria simultaneously. All objects with low [O III]/H $\beta$  ratios have high [O II]/[O III] ratios, so at least one of the two lines, [O II] or [O III], should therefore be detected.

In conclusion of this analysis, we argue that contamination by  $z = 0.61$  galaxies is unlikely to bias our sample significantly.

#### [O III] emitters at $z = 1.1$

At redshift 1.12, similar to the case above, the vast majority of the [O III] emitters in the comoving volume sampled by the NB filter will be detected in the optical bands. We use Fig. 13 of [Kakazu et al. \(2007\)](#) to estimate the number of [O III] emitters in our NB image to be around 100, assuming that the evolution in the [O III] LF between redshifts 0.83 and 1.1 is not dramatic, and considering that the line emission dominates the NB1060 flux. Contamination in our sample can only come from low luminosity, high  $EW$  [O III] emitters, unlikely to represent more than a handful of objects. Even so, for [O II] to remain undetected in the  $i'$  filter, a [O III]/[O II] ratio of 4 or higher is required at the detection limits of the  $i'$  and NB images. In the data presented in [Maier et al. \(2006\)](#) at redshifts between 0.4 and 3, no more than 5% of the galaxies have such high values. It is therefore unlikely that our sample is contaminated by [O III] emitters.

#### [O II] emitters at $z = 1.8$

Using the [O II] luminosity function of [Rigopoulou et al. \(2005\)](#), we estimate the number of [O II] emitters in our NB image to be  $\sim 300$  objects. The [O III] and H $\alpha$  lines at redshift 1.84 fall between the atmospheric windows that define the  $J$ ,  $H$  and  $K_s$  bands, and therefore do not contribute to the near-IR fluxes in these bands. Using the [Kennicutt \(1998\)](#) relations between the UV continuum and [O II] luminosity, we derive a rough estimate of the optical magnitudes expected for [O II] emitters at  $1.06 \mu\text{m}$ . At the flux limit of our data, we get  $m_{\text{opt}}^{\text{AB}} \approx 25.5$ , which is 2 to 3 mag brighter than the limiting magnitude of our optical data. Even with a large scatter around this value, we expect that the vast majority of [O II] emitters should be readily detected in the optical bands. Dusty starbursts may obviously have much fainter optical magnitudes, but such objects fall into the category of Extremely Red Objects, which, as explained above, can be discarded from their brightness in the  $K_s$  band. Very strong and unusual [O II]  $EW$ s would be required for dusty [O II] emitters to be selected as candidates without being detected in the  $K_s$  band, and such objects are likely to be spatially resolved.

We remark that [Taniguchi et al. \(2005\)](#) suggest that the few line emitters in their sample of  $z = 6.5$  LAE candidates resisting a definitive identification as LAEs could be [O II] emitters. Some, if not all, of these [O II] emitters would probably be detected in the  $K_s$  band with the same detection limit as ours. We therefore argue that contamination by [O II] emitters in our survey is likely to be low and unlikely to contaminate a large fraction of our sample.

#### 3.3.8. High-redshift LBGs

Bright high-redshift Lyman Break Galaxies (LBGs) can be detected in the NB1060 filter through their UV continuum. For this to happen, the redshift needs to be smaller than our target value of 7.7, but high enough for these objects to escape detection in the optical images, irrespective of the presence of Ly $\alpha$  emission. See [Cuby et al. \(2003\)](#) for such an example.

To estimate the level of contamination by these bright, high-redshift UV sources, we use the [Bouwens et al. \(2009\)](#) UVLFs at

$z \sim 6$  and  $\sim 7$ . As a worst case scenario, we consider two redshift ranges: the [6.0–7.0] range for which we use the  $z = 5.9$  UVLF and the [7.0–7.7] range for which we use the  $z = 7.3$  UVLF.  $I$  band dropouts may fail detection in the  $z$  band while being detected in the NB1060 filter. While the number of objects is much less than one in the second redshift range, it is  $\sim 3$  in the first redshift range. We consider this number to be significantly overestimated, because our simple calculation uses the luminosity function at  $z = 5.9$ , which applies to the lower bound of the redshift range and for which the luminosity is brighter. Had we used the  $z = 7.3$  UVLF to match the [6.0–7.0] range, we would have found 0.2 objects.

We note that these objects would – but for their possible detection in the  $z'$  band – pass all of our selection criteria, but could be mistaken as late type T-dwarfs (see Sect. 3.3.5). Interestingly, one of the brightest candidates in our sample (TDW#1), although primarily thought to be a T-dwarf, could also be a bright LBG.

#### 3.3.9. Conclusion

We have analyzed various possible sources of contamination for our sample. We remark that the magnitudes of our candidates are well distributed, and do not cluster towards the faint end of the luminosity range probed by our survey. This is in itself a sanity check demonstrating that we are not sensitive to a sudden increase of the false alarm rate towards faint fluxes. We note that we have made use of very robust selection criteria to select our candidates, consisting of very strong color breaks between the optical and the near-IR ( $\sim 3$  mag) together with additional near-IR criteria to reject EROs. We argue that our selection criteria are comparable to the criteria used in other LAE or LBG studies and we are therefore confident in the reliability of our sample. However, we cannot completely rule out contamination by one of the sources identified above, in particular artifacts and/or [O II] emitters. In the following, we will evaluate the impact on our conclusions from contamination of our sample, at the level of a couple of objects.

## 4. Discussion

### 4.1. Variance

The variance in the number of objects in our sample is due to Poisson errors and to fluctuations in the large scale distribution of galaxies. Various models to account for the effects of cosmic variance exist in the literature. [Trenti & Stiavelli \(2008\)](#) have developed a model that is offered as an on-line calculator. From this model and assuming a one-to-one correspondence between dark halos and LAEs, we obtain a value of  $\sim 28\%$  for the cosmic variance.

This result, however, strongly depends on the assumptions used to compute the level of completeness and contamination in our sample. In view of the limited number of objects in our sample and the large comoving volume ( $\sim 6.3 \times 10^4 \text{ Mpc}^3$ ), our results are probably limited more by Poisson noise –  $\sim 38\%$  for 7 objects – than by clustering. We note, however, that variance due to clumpy re-ionization is ignored and may also contribute to the total variance.

### 4.2. On the Ly $\alpha$ Luminosity function at $z = 7.7$

Before deriving constraints on the Ly $\alpha$  luminosity function of  $z = 7.7$  LAEs, we first apply a correction factor when converting NB1060 magnitudes to Ly $\alpha$  fluxes. From the  $J$  magnitude of

object LAE#1, we infer that  $\sim 70\%$  of the  $NB1060$  flux comes from the Ly $\alpha$  line, a value similar to the average value observed for the  $z = 6.5$  LAEs of Taniguchi et al. (2005), which corresponds to an  $EW_{\text{obs}}$  of  $\sim 110 \text{ \AA}$  in the observer frame. We adopt this ratio when deriving Ly $\alpha$  fluxes from  $NB1060$  magnitudes, and add a 0.1 magnitude rms error to account for the dispersion of this ratio between objects. This is consistent with the dispersion of the EW values of Taniguchi et al. (2005). Clearly, deeper  $J$  band imaging or spectroscopy would be required to estimate this fraction on a case by case basis.

We fit the Ly $\alpha$  luminosity function of our sample with a Schechter function,  $\Phi(L)$ , given by

$$\Phi(L)dL = \Phi^* \left(\frac{L}{L^*}\right)^\alpha \exp\left(-\frac{L}{L^*}\right) \frac{dL}{L^*}. \quad (8)$$

Considering the scarcity of datapoints in our sample, we do not fit all three parameters of the Schechter function simultaneously. Following Ouchi et al. (2008) and Kashikawa et al. (2006), we set the faint end slope of the luminosity function,  $\alpha$ , to  $-1.5$  and derive  $\Phi^*$  and  $L^*$  by simple  $\chi^2$  minimization. We note that there may be other functions more representative of the Ly $\alpha$  LAE LF at high redshifts. For instance, Kobayashi et al. (2007) derive numerical LFs from models of hierarchical galaxy formation. These LFs differ significantly from the Schechter function. However, for the sake of comparison with previous work, we keep the analytical Schechter formalism.

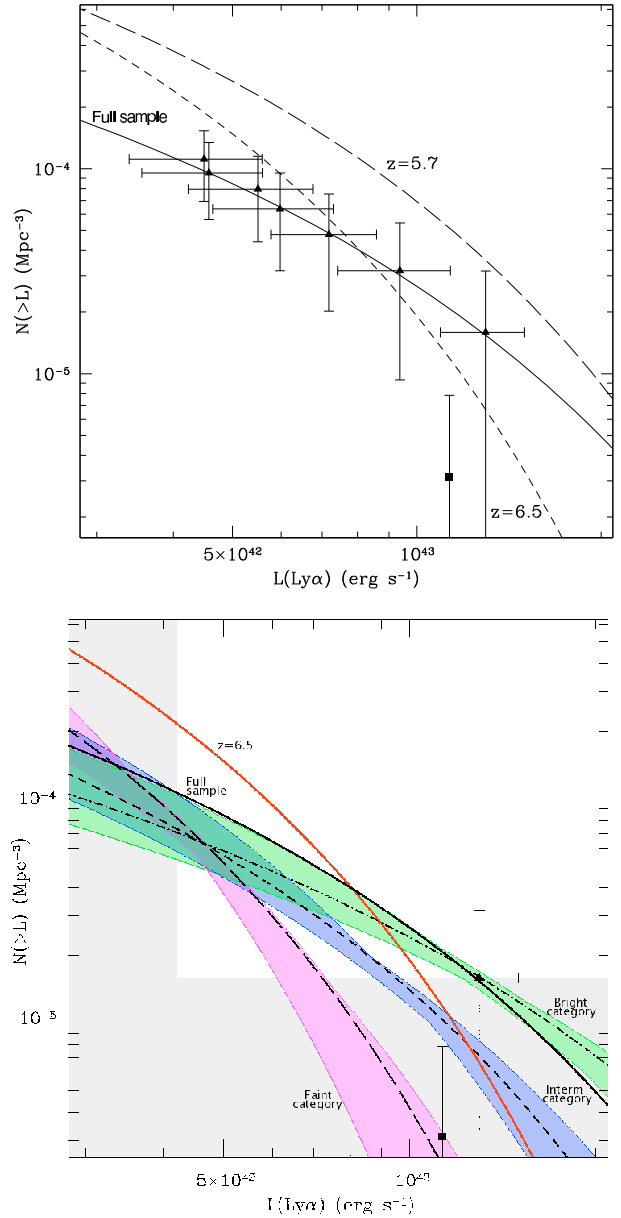
We initially assume that all 7 candidates, i.e., the *full sample*, are true  $z = 7.7$  LAEs, and derive the parameters of the corresponding LF. To evaluate the impact of sample contamination on the results, we then consider situations where only 4 of the 7 candidates are real. As discussed earlier in this paper, despite the robustness of our sample, we cannot completely rule out contamination from instrumental artifacts or peculiar low-redshift objects. We therefore conjecture that at least 4 objects in our sample are real  $z = 7.7$  LAEs, and evaluate the impact this conjecture has on the LF. To do this, we consider all possible subsamples consisting of 4 objects, and compute, for each subsample, the best fit parameters. The results of the fits for the full sample and the 35 subsamples are shown in Fig. 4.

Figure 4 shows that the fits of the 35 subsamples naturally divide into 3 different categories:

- a *bright* category of 20 samples containing the brightest object (LAE#1);
- an *intermediate* category of 10 samples that do not contain the brightest object but do contain the second brightest object (LAE#2);
- a *faint* category of 5 samples containing neither the brightest object nor the second brightest object.

For each sample, we compute the best fit Schechter LF with  $\alpha$  fixed to  $-1.5$ , and for each of the three categories defined above, we determine the average LF, which are reported in Table 4. The corresponding average LFs for each category are shown as dashed lines in Fig. 4. We note that the *full sample* LF (plain black line) corresponds very closely to the LF of the sample containing the four brightest objects. We also note that, by removing three objects from the *full sample* while keeping the brightest object in the *bright* category, we artificially increase  $L^*$ , or alternatively reduce  $\Phi^*$ . Consequently, the *full sample* LF is probably more representative of the case in which the brightest object is real than the average LF of the *bright* category.

To further illustrate our results in the light of the LAE LF at lower redshifts, we plot in Fig. 5 the error ellipses for the



**Fig. 4.** Cumulative Luminosity Functions (LFs) with  $\alpha = -1.5$ . *Upper panel:* luminosity function derived from the *full sample*. The data (triangles) are not corrected for completeness and a factor of 70% has been used to convert the  $NB1060$  fluxes into Ly $\alpha$  fluxes. The plain line is the best fit Schechter function through the datapoints. The  $z = 5.7$  (Ouchi et al. 2008, long dashed line) and the  $z = 6.5$  (Kashikawa et al. 2006, short dashed line) LFs are also plotted. The horizontal error bars include photometric uncertainties, including calibration uncertainties, and the dispersion attached to the conversion of  $NB1060$  magnitudes to Ly $\alpha$  line fluxes. The vertical error bars represent the Poisson noise associated to the number of candidates. The square point corresponds to the  $z = 6.96$  LAE of Iye et al. (2006). *Lower panel:* the shaded color areas represent the range of LFs in each of the three categories described in the text, and the dashed lines represent the associated average LFs. *Bright category:* green area and dot-dashed line; *intermediate category:* blue area and short-dashed line; *faint category:* magenta area and long-dashed line. Also plotted are the LFs at  $z = 6.5$  (Kashikawa et al. 2006, plain red line) and at  $z = 7.7$  LF (from the *full sample* of this work, plain black line). The square point is the  $z = 6.96$  LAE of Iye et al. (2006) and the triangle is LAE#1 (this work). The shaded grey areas to the bottom and left of the figure represent the regions where the  $z = 7.7$  LF would lie if none of our candidates were real LAEs.

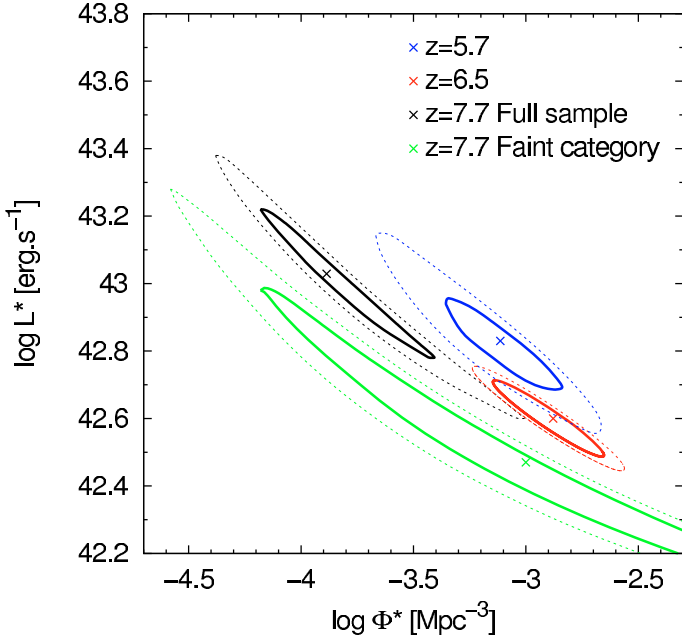


**Fig. 5.** Error ellipses for the best-fit Schechter parameters  $\Phi^*$  and  $L^*$  with  $\alpha$  fixed to  $-1.5$ . The solid and dotted lines represent the 68% and 95% confidence intervals, respectively. The *full* sample is plotted in black, the LF for the *faint* category is in green, the  $z = 6.5$  LF from Kashikawa et al. (2006) is in red and the  $z = 5.7$  LF from Ouchi et al. (2008) is in blue.

**Table 4.** Best fit Schechter LF parameters for  $\alpha = -1.5$ .

Redshift	$\log(L^*(\text{erg s}^{-1}))$	$\log(\Phi^*(\text{Mpc}^{-3}))$
7.7 <sup>a</sup>	$43.0^{+0.2}_{-0.3}$	$-3.9^{+0.5}_{-0.3}$
7.7 <sup>b</sup>	$43.3^{+0.6}_{-0.6}$	$-4.4^{+1.2}_{-0.7}$
7.7 <sup>c</sup>	$42.9^{+0.5}_{-0.7}$	$-3.8^{+2.1}_{-0.8}$
7.7 <sup>d</sup>	$42.5^{+0.5}_{-0.7}$	$-3.0^{+3.5}_{-1.2}$
6.5 <sup>(1)</sup>	$42.6^{+0.12}_{-0.16}$	$-2.88^{+0.24}_{-0.29}$
5.7 <sup>(2)</sup>	$42.8^{+0.16}_{-0.16}$	$-3.11^{+0.39}_{-0.31}$

**Notes.** <sup>(a)</sup> Full sample of 7 candidates. <sup>(b)</sup> Mean of the 20 *bright* subsamples. <sup>(c)</sup> Mean of the 10 *intermediate* subsamples. <sup>(d)</sup> Mean of the 5 *faint* subsamples (see text for details).

**References.** (1) Kashikawa et al. (2006); (2) Ouchi et al. (2008).

*full* sample and the *faint* category. Also plotted are the  $z = 6.5$  and  $z = 5.7$  LFs from Kashikawa et al. (2006) and Ouchi et al. (2008). The errors for the *faint* category are dominated by the fitting errors for each of the five LFs in the category. To account for the dispersion between samples we simply add the difference between the two most extreme LFs in the sample to the fitting error. The *full* sample LF indicates that the evolution in  $L^*$  and  $\Phi^*$  between  $z = 7.7$  and  $z = 6.5$  is opposite to the evolution between  $z = 6.5$  and  $z = 5.7$  at the  $2\sigma$  confidence level. Conversely, the *faint* category LF is consistent with evolution between  $z = 6.5$  and  $z = 5.7$  and with the  $z = 6.96$  datapoint of Iye et al. (2006). In other words, for our data to be consistent with other work we require that the two brightest objects in our sample are not real LAEs.

Only spectroscopic confirmation will allow one to draw firmer conclusions, which will still be based on small numbers and therefore subject to large uncertainties. Finally, we note that

the results remain qualitatively and quantitatively similar had we assumed that only 3 of our candidates were real instead of 4.

### 4.3. Implications

We used the model from Kobayashi et al. (2007) and our constraints on the LAE LF to estimate the ionization fraction of the IGM at  $z = 7.7$ . This model predicts the LAE LF as a function of the transmission to Ly $\alpha$  photons by the IGM, ( $T_{\text{Ly}\alpha}^{\text{IGM}}$ ), which is used as a global parameter. The Ly $\alpha$  attenuation by the IGM is a complex process involving the neutral fraction of hydrogen  $x_{\text{HI}}$  and the dynamics of the local IGM infall towards the LAEs (Santos 2004; Dijkstra et al. 2007). Within this model, the conversion factor from  $T_{\text{Ly}\alpha}^{\text{IGM}}$  to  $x_{\text{HI}}$  is therefore highly sensitive to the local density and dynamics of the IGM, and may not be representative of the *average* IGM. Using this model to fit our LFs within the range of observed luminosities, we derive values for  $T_{\text{Ly}\alpha}^{\text{IGM}}$  ranging from  $\sim 0.7$  for the *faint* category to 1.0 for the *full* sample.  $T_{\text{Ly}\alpha}^{\text{IGM}} \sim 0.7$  corresponds to  $x_{\text{HI}} \sim 0.3$  in the model of Santos (2004) for a given redshift of the Ly $\alpha$  line with respect to the systemic velocity of the galaxy. This  $x_{\text{HI}}$  value is similar to the one derived from the LAE Ly $\alpha$  LF at  $z = 6.5$  (Kobayashi et al. 2007).

Considering the high level of uncertainty of the  $z = 7.7$  LF derived from our results and of re-ionization models, we simply note here, in parallel to our earlier conclusions on the LF, that if one or both of our brightest objects is real, a low fraction of neutral hydrogen ( $\sim 0$ ) is inferred, in contradiction with earlier reports of an increasing fraction above  $z \sim 6$ . This conclusion still holds even if both of the brightest objects are not real, as long as a reasonable number of objects in our faint sample are real.

Finally, we note that other models that predict the evolution of the LF of high- $z$  LAEs are available in the literature (Baugh et al. 2005; Le Delliou et al. 2006; Cole et al. 2000; Mao et al. 2007; Thommes & Meisenheimer 2005; Mesinger & Furlanetto 2008), see also Nilsson et al. (2007) for a comparison of some of these models. These models add various ingredients into the simulations, and discussing our results in the light of each of these models is beyond the scope of this paper. For the sake of visual comparison, we plot in Fig. 6 our results corresponding to the extreme *full* sample and *faint* category compared to some of these models.

## 5. Conclusions

We used a deep  $1.06 \mu\text{m}$  narrow-band image obtained with WIRCam at CFHT to search for  $z = 7.7$  LAEs down to a Ly $\alpha$  luminosity limit of  $8.3 \times 10^{-18} \text{ erg s}^{-1} \text{ cm}^{-2}$ . The image totalled 40 hr of integration time, covered  $390 \text{ arcmin}^2$  and sampled a comoving volume of  $6.3 \times 10^4 \text{ Mpc}^3$ .

Using deep visible data of the field, we selected objects with a strong color break of up to 3 mag between the visible data and the NB1060 filter as LAE candidates. We obtained a sample of seven carefully selected candidates. We analyzed several sources of contamination, and argued that contamination is unlikely to affect all of our candidates.

We found that the Ly $\alpha$  LAE luminosity functions derived from our photometric sample, within the limitations of the Schechter formalism and with a fixed slope parameter  $\alpha = -1.5$ , would contradict the evolution in luminosity found by Kashikawa et al. (2006) between  $z = 5.7$  and  $z = 6.5$  at the  $1\sigma$  to  $2\sigma$  confidence level if either of the two brightest objects are real.

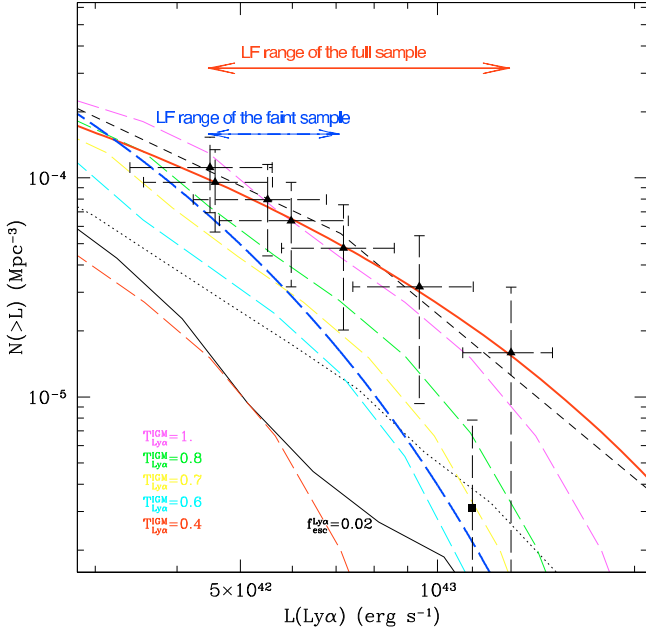


**Fig. 6.** Cumulative luminosity functions corresponding to the *full* sample (plain thick red line) and the *faint* category (long-dashed thick blue line). The range of luminosities sampled by the data for both samples are indicated by the arrows. Thin lines are  $z \sim 8$  LFs from various models: Baugh et al. (2005) (plain line), Mao et al. (2007) (dotted line), Thommes & Meisenheimer (2005) (short-dashed line), Kobayashi et al. (2007) (long-dashed color lines for various IGM Ly $\alpha$  transmissions  $T_{\text{Ly}\alpha}^{\text{IGM}}$ ) as indicated. The square point is the  $z = 6.96$  LAE of Iye et al. (2006).

To confirm these candidates as LAE, spectroscopic observations will be necessary.

Using models of Ly $\alpha$  LAE LFs available in the literature and our limits on the  $z = 7.7$  LAE LF we infer that the fraction of neutral hydrogen at  $z = 7.7$  is within the range [0.0–0.3].

*Acknowledgements.* The authors would like to thank the anonymous referee for constructive comments, which helped us to improve the precision and clarity of the paper; R. Ellis for granting us observing time at the Keck Observatory to attempt spectroscopy on an early candidate (which was later detected in the optical in a subsequent data release from the CFHTLS) and J. Richard for performing these Keck observations. We also thank J. Mao, A. Lapi, C. Baugh, A. Orsi, M. Kobayashi, E. Thommes, for providing their model data and M. Trenti and T. Totani for helpful discussions. We acknowledge support from the French Agence Nationale de la Recherche, grant number ANR-07-BLAN-0228.

## References

- Baugh, C. M., Lacey, C. G., Frenk, C. S., et al. 2005, *MNRAS*, 356, 1191  
 Becker, R. H., Fan, X., White, R. L., et al. 2001, *AJ*, 122, 2850  
 Bergström, S., & Wiklind, T. 2004, *A&A*, 414, 95  
 Bertin, E., & Arnouts, S. 1996, *A&AS*, 117, 393  
 Bouwens, R. J., Illingworth, G. D., Bradley, L. D., et al. 2009, *ApJ*, 690, 1764  
 Bouwens, R. J., Illingworth, G. D., Franx, M., & Ford, H. 2008, *ApJ*, 686, 230  
 Cimatti, A., Daddi, E., Mignoli, M., et al. 2002, *A&A*, 381, L68  
 Cole, S., Lacey, C. G., Baugh, C. M., & Frenk, C. S. 2000, *MNRAS*, 319, 168  
 Coupon, J., Ilbert, O., Kilbinger, M., et al. 2009, *A&A*, 500, 981  
 Cuby, J.-G., Le Fèvre, O., McCracken, H., et al. 2003, *A&A*, 405, L19  
 Cuby, J.-G., Hibon, P., Lidman, C., et al. 2007, *A&A*, 461, 911  
 Dijkstra, M., Lidz, A., & Wyithe, J. S. B. 2007, *MNRAS*, 377, 1175  
 Eyles, L. P., Bunker, A. J., Ellis, R. S., et al. 2007, *MNRAS*, 374, 910  
 Fan, X., Carilli, C. L., & Keating, B. 2006, *ARA&A*, 44, 415  
 Ilbert, O., Tresse, L., Zucca, E., et al. 2005, *A&A*, 439, 863  
 Ilbert, O., Arnouts, S., McCracken, H. J., et al. 2006, *A&A*, 457, 841  
 Ilbert, O., Capak, P., Salvato, M., et al. 2009, *ApJ*, 690, 1236  
 Iovino, A., McCracken, H. J., Garilli, B., et al. 2005, *A&A*, 442, 423  
 Iye, M., Ota, K., Kashikawa, N., et al. 2006, *Nature*, 443, 186  
 Kakazu, Y., Cowie, L. L., & Hu, E. M. 2007, *ApJ*, 668, 853  
 Kashikawa, N., Shimasaku, K., Malkan, M. A., et al. 2006, *ApJ*, 648, 7  
 Kennicutt, Jr., R. C. 1998, *ARA&A*, 36, 189  
 Kobayashi, M. A. R., Totani, T., & Nagashima, M. 2007, *ApJ*, 670, 919  
 Lawrence, A., Warren, S. J., Almaini, O., et al. 2007, *MNRAS*, 379, 1599  
 Le Delliou, M., Lacey, C. G., Baugh, C. M., & Morris, S. L. 2006, *MNRAS*, 365, 712  
 Lonsdale, C. J., Smith, H. E., Rowan-Robinson, M., et al. 2003, *PASP*, 115, 897  
 Maier, C., Lilly, S. J., Carollo, C. M., et al. 2006, *ApJ*, 639, 858  
 Mao, J., Lapi, A., Granato, G. L., de Zotti, G., & Danese, L. 2007, *ApJ*, 667, 655  
 Marigo, P., Girardi, L., Bressan, A., et al. 2008, *A&A*, 482, 883  
 Marmo, C. 2007, in *Astronomical Data Analysis Software and Systems XVI*, ed. R. A. Shaw, F. Hill, & D. J. Bell, *ASP Conf. Ser.*, 376, 285  
 Mesinger, A., & Furlanetto, S. R. 2008, *MNRAS*, 386, 1990  
 Nilsson, K. K., Orsi, A., Lacey, C. G., Baugh, C. M., & Thommes, E. 2007, *A&A*, 474, 385  
 Ota, K., Iye, M., Kashikawa, N., et al. 2008, *ApJ*, 677, 12  
 Ouchi, M., Shimasaku, K., Akiyama, M., et al. 2008, *ApJS*, 176, 301  
 Pickles, A. J. 1998, *PASP*, 110, 863  
 Pierini, D., Gordon, K. D., Witt, A. N., & Madsen, G. J. 2004, *ApJ*, 617, 1022  
 Richard, J., Pelló, R., Schaerer, D., Le Borgne, J.-F., & Kneib, J.-P. 2006, *A&A*, 456, 861  
 Richard, J., Stark, D. P., Ellis, R. S., et al. 2008, *ApJ*, 685, 705  
 Rigopoulou, D., Vacca, W. D., Berta, S., Franceschini, A., & Aussel, H. 2005, *A&A*, 440, 61  
 Ryan, Jr., R. E., Hathi, N. P., Cohen, S. H., & Windhorst, R. A. 2005, *ApJ*, 631, L159  
 Santos, M. R. 2004, *MNRAS*, 349, 1137  
 Stark, D. P., Ellis, R. S., Richard, J., et al. 2007, *ApJ*, 663, 10  
 Taniguchi, Y., Ajiki, M., Nagao, T., et al. 2005, *PASJ*, 57, 165  
 Thommes, E., & Meisenheimer, K. 2005, *A&A*, 430, 877  
 Tinney, C. G., Burgasser, A. J., & Kirkpatrick, J. D. 2003, *AJ*, 126, 975  
 Trenti, M., & Stiavelli, M. 2008, *ApJ*, 676, 767  
 Tresse, L., Maddox, S. J., Le Fèvre, O., & Cuby, J.-G. 2002, *MNRAS*, 337, 369  
 Willis, J. P., & Courbin, F. 2005, *MNRAS*, 357, 1348  
 Willis, J. P., Courbin, F., Kneib, J.-P., & Minniti, D. 2008, *MNRAS*, 384, 1039